



# Bridging the gap between H- and J-aggregates: Classification and supramolecular tunability for excitonic band structures in two-dimensional molecular aggregates F

Cite as: Chem. Phys. Rev. **3**, 021401 (2022); <https://doi.org/10.1063/5.0094451>

Submitted: 03 April 2022 • Accepted: 26 May 2022 • Published Online: 23 June 2022

 Arundhati P. Deshmukh,  Niklas Geue,  Nadine C. Bradbury, et al.

## COLLECTIONS

F This paper was selected as Featured



View Online



Export Citation



CrossMark



Applied Physics  
Reviews

Read. Cite. Publish. Repeat.

**19.162**  
2020 IMPACT FACTOR\*



# Bridging the gap between H- and J-aggregates: Classification and supramolecular tunability for excitonic band structures in two-dimensional molecular aggregates

Cite as: Chem. Phys. Rev. **3**, 021401 (2022); doi: [10.1063/5.0094451](https://doi.org/10.1063/5.0094451)

Submitted: 3 April 2022 · Accepted: 26 May 2022 ·

Published Online: 23 June 2022



View Online



Export Citation



CrossMark

Arundhati P. Deshmukh,<sup>1</sup>  Niklas Geue,<sup>1,2</sup>  Nadine C. Bradbury,<sup>1</sup>  Timothy L. Atallah,<sup>1,3</sup>  Chern Chuang,<sup>4</sup>  Monica Pengshung,<sup>1</sup>  Jianshu Cao,<sup>5</sup>  Ellen M. Sletten,<sup>1</sup>  Daniel Neuhauser,<sup>1</sup>  and Justin R. Caram<sup>1,a)</sup> 

## AFFILIATIONS

<sup>1</sup>Department of Chemistry and Biochemistry, University of California, Los Angeles, 607 Charles E. Young Dr. East, Los Angeles, California 90095, USA

<sup>2</sup>The Michael Barber Centre for Collaborative Mass Spectrometry, Manchester Institute of Biotechnology, The University of Manchester, 131 Princess Street, Manchester M1 7DN, United Kingdom

<sup>3</sup>Department of Chemistry and Biochemistry, Denison University, 500 West Loop, Granville, Ohio 43023, USA

<sup>4</sup>Department of Chemistry, University of Toronto, Toronto, Ontario M5S 3H6, Canada

<sup>5</sup>Department of Chemistry, Massachusetts Institute of Technology, Cambridge, Massachusetts 02139, USA

<sup>a)</sup>Author to whom correspondence should be addressed: [jcaram@chem.ucla.edu](mailto:jcaram@chem.ucla.edu)

## ABSTRACT

Molecular aggregates with long-range excitonic couplings have drastically different photophysical properties compared to their monomer counterparts. From Kasha's model for one-dimensional systems, positive or negative excitonic couplings lead to blue or red-shifted optical spectra with respect to the monomers, labeled H- and J-aggregates, respectively. The overall excitonic couplings in higher dimensional systems are much more complicated and cannot be simply classified from their spectral shifts alone. Here, we provide a unified classification for extended 2D aggregates using temperature dependent peak shifts, thermal broadening, and quantum yields. We discuss the examples of six 2D aggregates with J-like absorption spectra but quite drastic changes in quantum yields and superradiance. We find the origin of the differences is, in fact, a different excitonic band structure where the bright state is lower energy than the monomer but still away from the band edge. We call this an "I-aggregate." Our results provide a description of the complex excitonic behaviors that cannot be explained solely on Kasha's model. Furthermore, such properties can be tuned with the packing geometries within the aggregates providing supramolecular pathways for controlling them. This will allow for precise optimizations of aggregate properties in their applications across the areas of optoelectronics, photonics, excitonic energy transfer, and shortwave infrared technologies.

Published under an exclusive license by AIP Publishing. <https://doi.org/10.1063/5.0094451>

## INTRODUCTION

Excitonically coupled molecular aggregates are materials derived from chromophores whose optoelectronic behavior changes upon aggregation due to collective interactions of monomer transition dipole moments (TDMs). Such aggregates are represented in many natural and synthetic materials, including conjugated polymers, supramolecular chromophore assemblies, and photosynthetic complexes.<sup>1,2</sup> Extended aggregates of chromophores have found applications in many areas—energy transfer,<sup>1,3,4</sup> polaritonics, or plexitonics,<sup>5–8</sup> a

variety of optoelectronic devices, such as luminescent solar concentrators, organic light emitting diode (OLEDs),<sup>9,10</sup> and shortwave infrared technologies (SWIR, 1000–2000 nm).<sup>11–13</sup> In extended aggregate systems, the huge enhancements of TDMs from monomers to aggregates result in excitonic superradiance, wherein a large number of in-phase TDMs lead to collective emission phenomena. Superradiance can be useful in modulating exciton transport and telecommunication related applications.<sup>13,14</sup> These applications can require high quantum yields and efficient energy/charge transfer, which, in turn, directly depend on

the underlying exciton band structure. Therefore, elaborating structure-property relationships for the excitonic band structures will allow for supramolecular tunability of such properties, enabling the rational design of molecular aggregates.

In the 1950s, Kasha developed a framework to relate the excitonic shifts in the optical spectra of molecular aggregates to the underlying structure. Within this framework, when the transition dipoles are arranged head-to-tail, the excitonic state with all dipoles oscillating in-phase (with the wavevector  $k = 0$ ) is lowered in energy compared to the monomer. This leads to a red shift in the optical transitions. 1D excitonic systems with such head-to-tail arrangements are called J-aggregates.<sup>15</sup> This  $k = 0$  state is the “bright state” as it has the highest transition probability based on Fermi’s golden rule.<sup>2</sup> Conversely, co-facial arrangement leads to blue-shifted transitions as the bright state is higher in energy than the monomer, known as H-aggregates. All other arrangements result in Davydov splitting with two dipoles per unit cell, producing two excitonic peaks for any single set of electronic transitions.<sup>16,17</sup> J-aggregates are typically characterized by enhanced quantum yields from their respective monomers, high radiative rates, and narrow linewidths.<sup>1,18</sup> In cases where the net TDM is enhanced compared to the monomer, J-aggregates can show excitonic superradiance. H-aggregates, on the other hand, usually have low quantum yields as non-radiative relaxation to the dark band edge excitonic state dominates the excited state decay.<sup>1</sup>

Kasha’s model arises from considering only dimers and one-dimensional chains as well as nearest neighbor dipolar interactions. These limitations lead to the model’s failure in describing systems with permanent dipole moments,<sup>19</sup> charge transfer or quadrupolar excitonic coupling,<sup>20</sup> or higher dimensional aggregates, e.g., sheet-like and tubular aggregates.<sup>21–23</sup> Examples of non-Kasha behavior have also been observed in polydiacetylene, poly(3-hexylthiophene), and other conjugated polymers, referred to as segregated “HJ” aggregates, wherein interchain and intrachain couplings have opposite signs.<sup>24,25</sup> In some cases, different forms of couplings can cancel out, resulting in a null aggregate with no excitonic shift in optical spectra despite a significant excitonic bandwidth.<sup>26,27</sup>

Using the Frenkel exciton model with only long-range dipole-dipole couplings,<sup>28</sup> we have previously shown the presence of “I-aggregates” in 2D lattices.<sup>22</sup> We define I-aggregates with an excitonic band where the bright state is red-shifted from the monomer but still has dark states below drawing characteristics from both H- and J-aggregates. We showed that such behaviors depend upon the relative slip between adjacent monomers in the 2D lattices [Fig. 1(a)]. I-aggregates have red-shifted aggregate to monomer absorption (J-like) and yet typically suppressed quantum yields (H-like).<sup>22</sup> J-aggregates, on the other hand, should have a bright state at the band edge (or within  $k_B T$  from the band edge where  $k_B$  is Boltzmann constant). Therefore, J-aggregates will have enhanced radiative rates with respect to the monomers, which further increase at low temperatures. J-aggregates will also show persistent excitonic superradiance due to simultaneous increase in quantum yields and reduced excited state lifetimes. Since I- and J-aggregates both show aggregate to monomer redshifts, a more comprehensive classification system for 2D aggregates is needed. Here, we demonstrate the distinct possibilities of excitonic band structures in 2D aggregates and their experimental signatures. Pathways for chemically tuning these excitonic band structures are necessary to access a breadth of photophysical properties in

molecular aggregates as well as to optimize material properties for specific applications. For example, chemically tuning the band structures from a non-band edge I-aggregate to band edge J-aggregate will enable aggregates with high quantum yields, a prerequisite for many applications.<sup>29,30</sup>

Red-shifted aggregates with non-band edge bright states have been reported in several other systems. Notable examples include the asymmetric aspect ratios of perylene bisimide crystals,<sup>21</sup> molecules with quadrupolar moments,<sup>31</sup> and the well-known HJ aggregates with intrachain coulombic coupling and interchain charge-transfer coupling.<sup>24</sup> A distinguishing property of the I-aggregates from the aforementioned examples is that we only consider long-range dipole-dipole couplings in two dimensions where the positive and negative contributions are encoded within the nanoscale geometry of the aggregate, which can be modulated via supramolecular chemistry. Another related example is the natural antenna complex LH2, where the lowest energy  $k = 0$  state is optically dark due to the periodic boundary conditions imposed by the ring geometry and the second lowest energy  $k = \pm 1$  state is bright.<sup>32,33</sup> This state is usually within  $k_B T$  from the lowest state at room temperature (RT). In contrast, the I-aggregates always have a  $k = 0$  bright state. Due to the nature of 2D dipole-dipole couplings, the  $k = 0$  is no longer the lowest in energy for certain geometries and usually thermally inaccessible from the band edge at room temperature.

We start with a detailed discussion of the theoretical basis for excitonic band structures of 2D aggregates provided by Chuang *et al.*<sup>34</sup> The positive or negative contributions of short- and long-range couplings lead to critical differences in the band structures which have distinct spectroscopic signatures in emission and temperature dependent properties. Based on this, we provide a classification system for 2D aggregates based on aggregate to monomer shifts, temperature dependent peak shifts and broadening, as well as quantum yield enhancements. We measure quantum yields, lifetimes, superradiance, temperature dependent peak shifts, and full-width at half maximum (FWHM) across a set of 2D aggregates of six closely related cyanine dyes. Stochastic Hamiltonian modeling allows for rapid screening of the large parameter space for aggregate geometries and disorders, relating the observed photophysical properties to the underlying geometries. We show that such differences in the band structures and ultimately, the photophysical properties, can be manipulated with the supramolecular packing of the chromophores within the extended 2D structures. The relative slip between adjacent monomers as well as length of the monomer determines the relative contributions of short- and long-range couplings, which in turn, result in the distinct excitonic band structures of H-, I-, and J-aggregates. This leads to an internally consistent description of the distinct photophysical behaviors—enhanced or suppressed quantum yields relative to their monomers, differences in superradiance and red or blue shifts with temperature. Our findings can be utilized to rationally design molecular excitonic systems with tunable photophysical properties, enabling the optimization of material properties for specific applications.

## RESULTS AND DISCUSSION

We calculate the excitonic density of states (DOS) and the bright state energy using the Frenkel exciton Hamiltonian with the brick layer model. Within this model, we treat each monomer as a brick with a given dipole moment ( $\mu$ ), length ( $L$ ), width ( $w$ ), and tile them

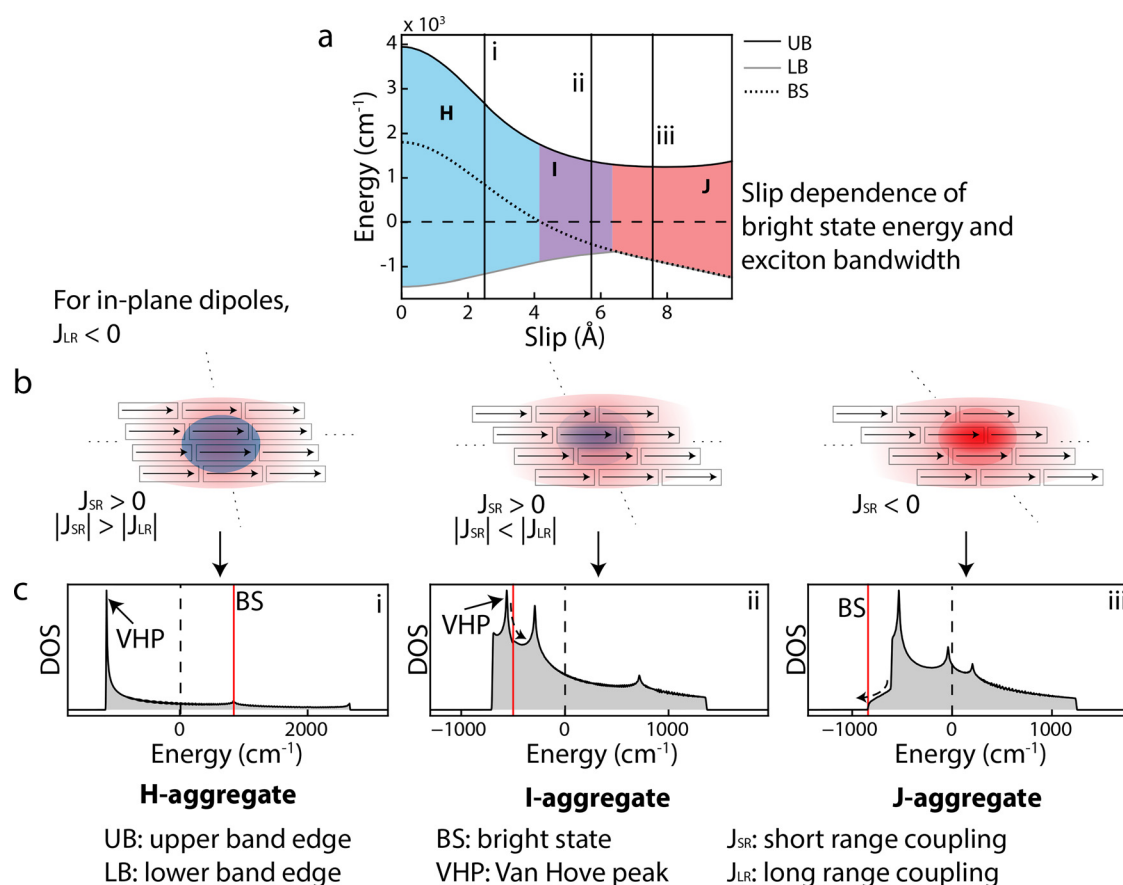


**FIG. 1.** (a) Bandwidth of the exciton DOS and position of the bright state (dotted line) as a function of slip in two-dimensional (2D) aggregates; the dashed line indicates monomer energy. Blue region: the bright state higher in energy than monomer (H-aggregate), purple region: the bright state lower in energy than monomer but away from the lower band edge (I-aggregate), and red region: the bright state lower in energy than the monomer and at the band edge (J-aggregate), (b) schematic showing possibilities of short- and long-range couplings for 2D aggregates with in-plane dipoles leading to H-, I-, and J-aggregates, (c) representative excitonic DOS for slips corresponding to the vertical lines i, ii, and iii in part (a) showing H-, I-, and J-aggregate band structures, respectively. The red solid line indicates bright state energy, and the dashed line indicates monomer energy. Curved dashed arrows indicate the direction of temperature dependent shifts. Calculations were performed on  $405 \times 405$  aggregate with a disorder of  $100 \text{ cm}^{-1}$ ,  $1.8 \text{ D}$  transition dipole moment, and  $21.6 \times 4.0 \text{ \AA}$  brick size.

in a 2D brick layer lattice with different slips ( $s$ ).<sup>22,28,35</sup> The eigenvalues of this Hamiltonian provide the excitonic DOS and Fermi's golden rule gives the bright state. See the [supplementary material](#) for computational methods and Fig. S1 for details. Table S1 lists the parameters used in the model. In Fig. 1(a), we plot the bright state, upper and lower band edge of the DOS for a 2D brick layer aggregate with varying slip values. As we increase the slip, the band structure goes from H-aggregate (bright state blue-shifted from the monomer), to I-aggregate (bright state red-shifted but away from the band edge), and finally to J-aggregate (bright state at the lower band edge).

### Significance of short- and long-range couplings

Prior theory by Chuang *et al.* explains the origin of H-, I-, and J-aggregate behaviors on the basis of the types of short- and long-range couplings in 2D aggregates.<sup>34</sup> The possible short- and long-range couplings for a 2D aggregate with in-plane TDMs are explained in Fig. 1(b). Long-range interactions in extended 2D systems with

in-plane TDMs always contribute a net negative coupling ( $J_{LR} < 0$ ). Short range interactions can either be positive or negative depending on the relative slip, orientation, and the coupling model. In cases where the short-range couplings are positive and higher in magnitude than the long-range couplings, we obtain a 2D H-aggregate. All slip values in the blue region of Fig. 1(a) show this behavior. In Fig. 1(c), we show a representative example of the excitonic DOS for a slip value denoted with roman numeral "i" in Fig. 1(a). Since there is always some negative contribution in 2D lattices, the bright state is never at the upper band edge.<sup>34</sup> When the short-range coupling is positive, but smaller than the long-range coupling, the bright state is red-shifted from the monomer but still has lower energy dark states below, making it an I-aggregate. The overall coupling, in this case, is negative resulting in red-shifted aggregate to monomer absorptions. This is denoted by the purple shaded region in Fig. 1(a), and a representative DOS is shown in Fig. 1(c) corresponding to the slip denoted by "ii." For a 2D J-aggregate, both the short- and long-range couplings are negative, making the bright state also the lowest energy state in the

excitonic DOS, similar to Kasha's model. This scenario is shown in the red shaded region in Fig. 1(a), and a representative DOS in Fig. 1(c) (denoted by "iii").

As shown in Fig. 1(c), the 2D excitonic DOS has several sharp features, or Van Hove Peaks (VHPs). VHPs arise from extrema in the dispersion relations where the dispersion curve is flat, i.e.,  $\frac{dE}{dk} = 0$  (in the 2D case, the extrema are saddle points in the dispersion curves). Effectively, a VHP consists of a large number of states concentrated in a close energy range. In other 2D materials (e.g., graphene), this is known to cause superconductivity, topological insulation, and other exotic phenomena.<sup>36–38</sup> In the case of the molecular aggregates, the position of the bright state relative to the VHPs can be useful in distinguishing I-aggregates from J-aggregates and ultimately, explaining many of the photophysical properties such as quantum yields, linewidths, temperature dependent shifts, and transport properties.

Chuang *et al.* also provide relationships between the position of the bright state relative to the VHP and temperature dependent peak shifts.<sup>34</sup> For bright states lower in energy than the VHP, the local slope

of the DOS is positive, meaning that there are more dark states on the higher energy side of the bright state than on the lower energy side. With increasing temperature, this asymmetric distribution of the dark states near the bright state pushes the bright state away toward lower energy, resulting in a red shift. Thus, the positive slope near the bright state results in a red shift with increasing temperature [indicated by dashed arrows in Fig. 1(c)]. Conversely, for bright states higher in energy than the VHP, the local slope of the DOS is negative with a relatively higher number of states below the bright state, and thus, we observe a temperature dependent blue shift.

### Classification scheme for 2D aggregates

Such distinct possibilities in 2D aggregates suggest that excitonic peak shifts alone are not diagnostic of the band structure, coupling strength, and emissivity. To probe higher dimensional aggregate structures, one must go beyond aggregate to monomer absorption peak shifts and narrowing. Expanding on previous theories,<sup>22,34</sup> we present

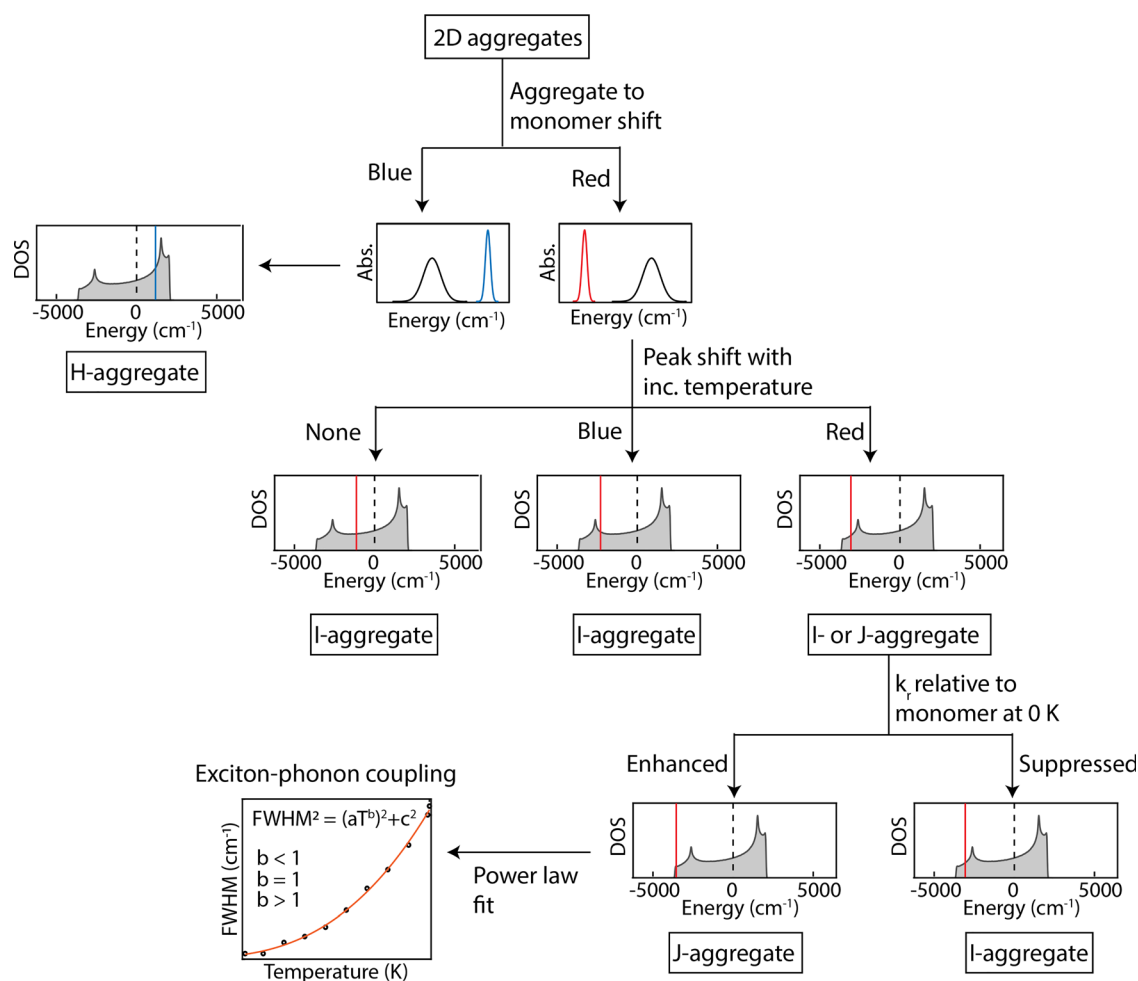


**FIG. 2.** Schematic of the classification scheme for two-dimensional excitonic aggregates based on aggregate to monomer shifts, temperature dependent shifts, and radiative rate ( $k_r$ ) enhancement from the monomers. Dashed vertical lines indicate monomer energy, and vertical colored lines indicate bright states.

a classification system encompassing such diverse excitonic behaviors in 2D aggregates based on peak shifts and peak broadening with temperature as well as room temperature quantum yields. The following paragraph and Fig. 2 summarize our classification system.

For 2D aggregates, a blue-shifted absorption from aggregate to monomer indicates H-aggregation, whereas, for aggregates with red-shifted absorptions from their monomers, both I- and J-aggregation is possible. The position of the bright state with respect to the VHPs contributes to the temperature dependent properties. For band edge J-aggregates, the local slope of the DOS is always positive. Therefore, band edge J-aggregates must show red-shifts with increasing temperature, whereas I-aggregates can show red, blue, or no shifts with temperature depending on the local slope (positive, negative, or zero, respectively) of the DOS near the bright state. As a result, a blue or not shifting aggregate peak with temperature can be conclusive evidence for an I-aggregate. Temperature dependent redshift along with enhanced radiative rate from the monomer can be conclusive evidence for J-aggregates.

Changes in quantum yields with temperature can also be related to I- or J-aggregation behavior based on the thermal occupation of the bright state. In band edge J-aggregates, one expects a decreasing quantum yield upon heating as the occupation number of the lowest energy bright state will decrease with temperature. For non-band edge I-aggregates, higher temperatures enable occupation of higher energy states leading to increasing quantum yield upon heating. For J-aggregates, temperature dependent power laws can inform on exciton-phonon coupling processes that lead to thermal broadening (discussed in detail later). Furthermore, the amount of thermal broadening can also be used as a relative measure of the total distance of the bright state from the band edge (also discussed in detail later).<sup>22</sup> Overall, these properties form a complete description of the distinct behaviors possible in 2D excitonic systems, where each experimental observable (quantum yields, temperature dependent shifts and broadening power laws) can be related to a specific aspect of the excitonic band structure.

We demonstrate examples of the distinct excitonic band structures across 2D aggregates of six dyes with different polymethine bridge lengths (Cy3, Cy5, and Cy7; Cy = cyanine) and substitutions on the central position, shown in Fig. 3(a). In our earlier work, thermodynamic control of the aggregate self-assembly enabled selective stabilization of each aggregate morphology via an interplay of concentration, solvent:non-solvent ratio, and dielectric screening. Using this approach, we were able to stabilize the 2D sheet-like morphology of all the dyes studied here (supplementary material, Fig. S3).<sup>39</sup> We also include the well-known dye 3,3'-bis(4-sulfobutyl)-5,5',6,6'-tetrachloro-1,1'-diethylbenzimidacarbocyanine, sodium salt (TDBC), commonly used in photonic applications.<sup>40,41</sup> All 2D aggregates are prepared by injecting a methanol solution of the dye in water or aqueous NaCl (see the Experimental section for exact conditions), followed by equilibration in the dark for 24 h. By changing the dye lengths as well as substitutions on the central position of the cyanine bridge [Fig. 3(a)], we afford extended 2D aggregates with different brick lengths and slips. As shown in Fig. 1 and previous works, these parameters lead to subtle variations in the excitonic band structure.<sup>23,34</sup> The absorptions of these 2D aggregates range from 587 nm (TDBC) to 1050 nm (Cy7-DPA), as shown in Fig. 3(b). The narrow line shape with a high energy tail observed across all aggregates is characteristic of extended 2D aggregate structures and is also seen in other 2D aggregates, e.g., perylene bisimides.<sup>42</sup>

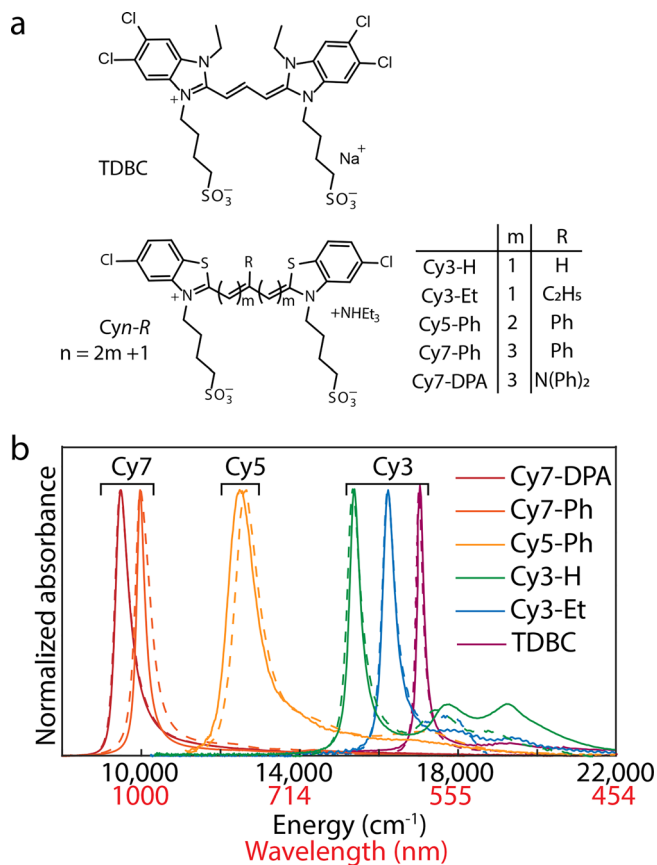
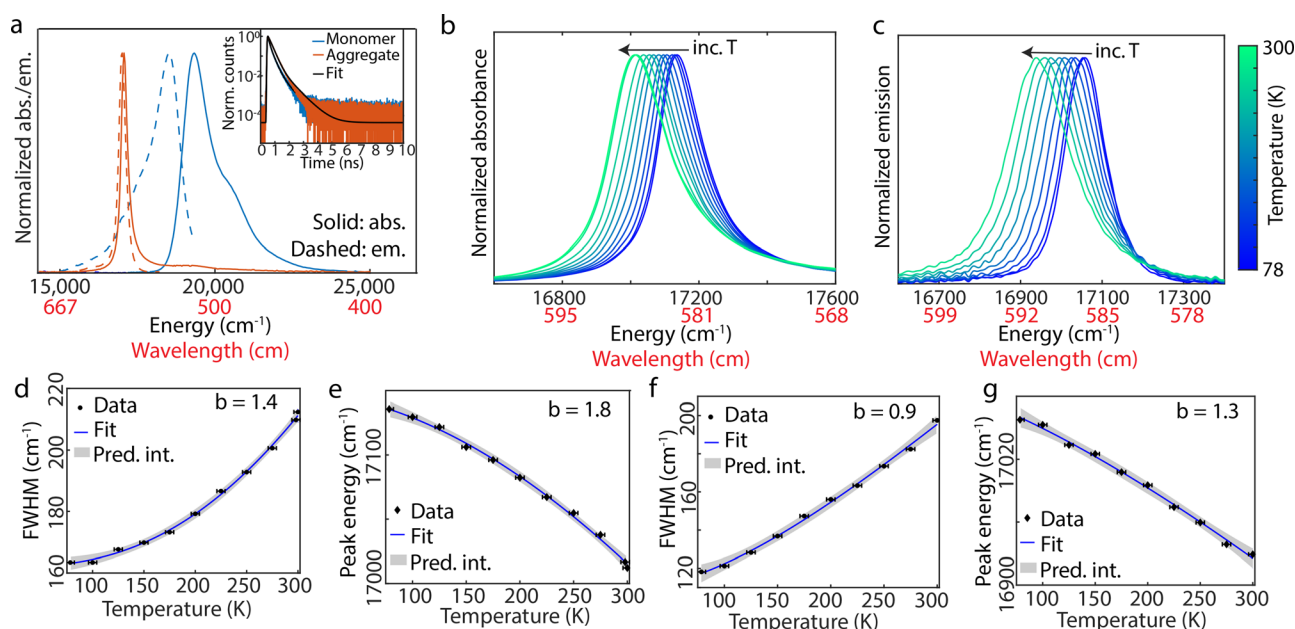


FIG. 3. (a) Structure of the six dyes explored in this work—benzimidazole cyanine dye TDBC and benzothiazole cyanine with varying central position substitutions and bridge lengths, (b) absorption spectra of all the aggregates in solutions (solid lines) and dried 1:1 (w/w) sucrose:trehalose sugar matrix (dashed lines). All aggregate solutions are in water-methanol or aqueous NaCl-methanol mixtures.

### Quantum yield and superradiance

We measure the emissive properties of all the aggregates at room temperature (RT). We highlight TDBC as an archetypal example in Fig. 4 owing to the narrowest absorption linewidth [Fig. 3(b)] and the highest quantum yield of aggregate (discussed later in Table I). As seen from the solution absorption and emission spectra in Fig. 4(a), TDBC aggregate (red) has narrowed absorption and emission compared to the monomer (blue) and very small Stokes shift ( $\sim 2$  nm).<sup>1</sup> Figure 4(a) inset shows the time-correlated single photon counting (TCSPC) histograms for both the monomer and aggregate of TDBC. Absolute quantum yields and lifetimes in RT solutions for all the monomers and aggregates across the library are shown in Table I (see supplementary material, Fig. S4 and Table S2 for all absorption, emission spectra, and lifetimes of the additional aggregates). All the monomer absorption spectra in Fig. S4, including the Cy7 dyes, have the characteristic line shape of the “cyanine form,” indicating the absence of any symmetry breaking and bond length alternation.<sup>43–45</sup>

We calculate the radiative rates for all the aggregates and monomers from lifetimes and quantum yields of each sample. We define excitonic superradiance ( $\eta_{SR}$ ) as



**FIG. 4.** (a) Normalized absorption (solid lines) and emission (dashed lines) spectra for TDBC monomer (blue) and TDBC aggregate (red). Inset: Time correlated single photon counting data for TDBC monomer (blue), and TDBC aggregate (red) with biexponential fits in black, (b)–(g) temperature dependent spectroscopy data for TDBC aggregate in sugar matrix from 78 to 300 K, (b) normalized absorption spectra, (c) normalized emission spectra, (d) absorption full-width at half-maximum (FWHM), (e) absorption peak energy, (f) emission FWHM, and (g) emission peak energy. Fits are from Eqs. (3) and (4) for FWHM and peak energies, respectively. Error bars are estimates of  $\pm 2$  K. Grey region indicates 95 % prediction interval.

$$\eta_{SR} = \frac{\mu_{agg}^2}{\mu_{mon}^2}, \quad (1)$$

where  $\mu_{agg}$  and  $\mu_{mon}$  are the transition dipole moments of aggregate and monomer, respectively. Other definitions of superradiance exist in the literature,<sup>21,46</sup> and superradiance factor as high as 62 has been reported for thiocarbocyanine J-aggregates using previous metrics.<sup>46</sup> However, these do not account for the effects of the energy gap law.<sup>47</sup> We use Eq. (1), which includes the effects of drastic changes in energy gaps between aggregates and monomers using the following equation:

$$\mu^2 = \frac{\Phi 3\pi\epsilon_0\hbar^4 c^3}{\tau n E_g^3}, \quad (2)$$

**TABLE I.** Emissive properties of all the dye monomers and 2D aggregates in solutions at room temperature. Lifetimes ( $\tau$ ), quantum yields ( $\phi$ ), and transition dipole moments ( $\mu$ ) for all monomers (subscript *mon*) and aggregates (subscript *agg*) along with superradiance rates ( $\eta_{SR}$ ) calculated using Eqs. (1) and (2) are shown. Errors on quantum yields are standard deviations across three samples.

Dye	$\tau_{mon}$ (ps)	$\tau_{agg}$ (ps)	$\Phi_{mon}$ (%)	$\Phi_{agg}$ (%)	$\mu_{mon}$ (D)	$\mu_{agg}$ (D)	$\eta_{SR}$
TDBC	80	150	$2.8 \pm 0.2$	$49 \pm 3$	13	40	9
Cy3-Et	60	195	$0.31 \pm 0.03$	$14 \pm 2$	5	20	18
Cy3-H	268	207	$5.7 \pm 0.6$	$13 \pm 4$	10	20	4
Cy5-Ph	467	229	$9.2 \pm 0.5$	$0.028 \pm 0.005$	12	1	0.008
Cy7-Ph	410	...	$4.4 \pm 0.2$	...	11	...	...
Cy7-DPA	637	...	$2.3 \pm 0.2$	...	7	...	...

where  $\Phi$ ,  $\tau$ ,  $n$ , and  $E_g$  denote the quantum yield, lifetime, refractive index, and energy gap, respectively. We approximate the energy gap as the mean of absorption and emission peak energies.

All the Cy3 dye aggregates have significantly enhanced quantum yields at RT as compared to their respective monomers, with TDBC showing the highest  $\Phi_{agg} = 49 \pm 3\%$  (17 times higher than the monomer). On the other hand, the quantum yield of the Cy5-Ph aggregate was found to be suppressed from the monomer. Both the Cy7 dyes had very low quantum yields that were below our detectable limit ( $<0.01\%$ ). All the Cy3 dye aggregates were also superradiant indicating enhanced transition dipole moments in the aggregates. TDBC and Cy3-Et aggregates were superradiant in spite of having higher aggregate lifetime than the monomer. However, the overall transition dipole moments weighted by the energy gap were still enhanced for these two aggregates as compared to their respective monomers. In the case of TDBC, aggregate lifetime is 1.8 times higher than that of the monomer (without even accounting for the lower energy gap effects) but the quantum yield is about 17 times higher. Cy5-Ph aggregate had a suppressed transition dipole moment from its monomer, mainly attributed to the two orders of magnitude lower quantum yield than the monomer. A notable point is that according to the traditional H- and J-aggregate classification based on aggregate to monomer shifts, all these aggregates would be J-aggregates despite the significant differences in their emissive properties (supplementary material Fig. S4).

### Temperature dependent peak shifts

To investigate the origins of such differences, we use temperature dependent spectroscopy. We stabilize all the 2D aggregates in a 50:50

(w/w) sucrose:trehalose sugar matrix, following a previously reported procedure.<sup>48</sup> Sugar matrix stabilization protects the aggregate morphologies at low temperature so that other possibilities like the changes in the aggregate structure itself can be ruled out. Moreover, the frustrated packing afforded by structural mismatch between the sugars keeps the samples optically transparent by forming a glassy matrix. Figure 3(b) shows the absorption spectra of all J-aggregates in a sugar matrix (dashed lines) superimposed with their solution spectra (solid lines). We do not observe major changes in the lineshapes or peak positions indicating that the overall aggregate morphologies are still intact. In some cases, there is a slight broadening (Cy7-Ph) or shift (Cy5-Ph) in the sugar matrix, indicative of additional disorder though it is minor compared to the overall line shape.

We conduct temperature dependent absorption spectroscopy on all the sugar matrix stabilized aggregates, along with temperature dependent emission for all the aggregates with detectable quantum yields. Figures 4(b)–4(g) show one complete dataset for TDBC while those for the other dyes can be found in supplementary material, Figs. S5–S8. For TDBC, we observe that the aggregate peak red-shifts and broadens as we increase the temperature from 78 to 300 K [Figs. 4(b) and 4(c)]. Summarized in Table II, all the Cy3 and Cy5 aggregates including TDBC redshift with increasing temperature while the Cy7 aggregates show blue or no shift (supplementary material Fig. S5).

The red-shifting behavior for all Cy3 dyes implies a bright state that is lower in energy than the VHP. The high superradiance values (due to enhancement of radiative rates) suggest that they are not only at lower energy than the VHP but are also at the band edge. Therefore, we classify all the Cy3 aggregates including TDBC as Kasha's J-aggregates with band edge bright states. In contrast, Cy5-Ph aggregates have a red shifting peak with temperature even though the radiative rate is suppressed from the monomer as indicated by  $\eta_{SR} < 1$ . This implies that the bright state of Cy5-Ph is at lower energy of the VHP but still has significant dark states below such that non-radiative pathways dominate the excited state decay. Therefore, we classify Cy5-Ph as an I-aggregate with a bright state lower in energy than the VHP. All the Cy3 and Cy5 aggregates show similar trends in temperature dependent emission as well, where the aggregate peaks red shift with increasing temperature (supplementary material Figs. S7 and S8). We cannot completely rule out the possibility of exciton trapping in the temperature dependent emission spectra.<sup>49–51</sup> However, a monotonic red shift with similar power laws in both absorption and emission

**TABLE II.** Summary of temperature dependent absorption data for 2D aggregates. Power laws [ $b$  parameter from Eq. (3) for FWHM and  $b_0$  from Eq. (4) for peak energies] and direction of temperature dependent peak shifts. Errors are from 95% confidence intervals.

Dye	Peak shift with increasing temperature	Power law for FWHM ( $b$ )	Power law for peak energies ( $b_0$ )
TDBC	Red	$1.4 \pm 0.2$	$1.8 \pm 0.3$
Cy3-Et	Red	$0.9 \pm 0.1$	$1.0 \pm 0.2$
Cy3-H	Red	$1.0 \pm 0.2$	$1.1 \pm 0.6$
Cy5-Ph	Red	$1.0 \pm 0.2$	$1.1 \pm 0.3$
Cy7-Ph	None	...	...
Cy7-DPA	Blue	...	...

hints that exciton trapping is not the dominant process in the studied temperature range.

Recalling Fig. 2, the temperature dependent shifts are sensitive to the local slope of the DOS.<sup>34</sup> Therefore, Cy7-Ph, which showed no shift (supplementary material Fig. S5), must have a bright state farther from the band edge in a relatively flat region between the VHPs. Since Cy7-DPA is blue shifting with temperature, it has a bright state at higher energy than the VHP (or locally negative slope of the DOS). Therefore, we classify both Cy7 cases as I-aggregates.

These observations are also consistent with our previous studies where we used a thermal broadening based metric to conclude that both Cy7 aggregates were I-aggregates. Furthermore, Cy7-Ph has a bright state farther away from the band edge as compared to Cy7-DPA.<sup>22</sup> The relative distance of the bright state from the band edge can be qualitatively gauged by means of the amount of thermal broadening. In cases where the bright state so far from the band edge that it is thermally inaccessible, one expects no broadening (irrespective of the relative position to the VHP), as in the Cy7-Ph aggregate (supplementary material Fig. S5). Cy7-DPA shows thermal broadening despite being an I-aggregate, meaning that the bright state is relatively closer to the band edge.

### Temperature dependent power laws

In band edge J-aggregates, thermal line broadening and shifts are modeled using exciton-phonon coupling with the environment, previously described with power laws which uniquely reflect the combination of exciton DOS and exciton-phonon coupling spectral density (also called as system-bath coupling).<sup>49,52–55</sup> Linewidths can be thought of as the sum of rates of various phonon assisted exciton scattering processes. The rates are a result of energy conservation between the system and the surrounding bath, as well as the couplings between the two. The latter is a constant for homogenous, translationally symmetric systems while the former gives a weighted average of system-bath DOS, and therefore the power law dependence. Such power law scalings of FWHM and peak shifts can be used as an indicator for the types of underlying exciton-phonon coupling processes. We fit the extracted linewidths and peak energies to power laws as shown in Figs. 4(d)–4(g). The following Eqs. (3) and (4) were used for fitting the FWHM ( $\omega$ ) and peak energies ( $\nu_0$ ), respectively,

$$\omega^2 = (aT^b)^2 + c^2, \quad (3)$$

$$\nu_0 = a_0 T^{b_0} + c_0. \quad (4)$$

The first terms denote the homogeneous contributions following a power law ( $b$ ,  $b_0$  for FWHM and peak energies, respectively) while the second term ( $c$ ,  $c_0$  for FWHM and peak energies, respectively) denotes the extrapolated inhomogeneous limit at 0 K (details in supplementary material, Sec. 3). Table II summarizes the power laws obtained from temperature dependent absorptions for all band edge aggregates. The corresponding power law fits for the rest of the aggregates are shown in supplementary material, Fig. S6.

Despite similar excitonic shifts and energies, we find that the benzothiazole aggregates display a different power-law dependence in its spectral shift and FWHM compared to the benzimidazole dye TDBC aggregate. We hypothesize that the different heterocycles and additional alkyl group result in a modified phonon DOS for TDBC. The power laws observed here for 2D aggregates are lower than those

reported for other 1D and quasi-1D systems such as light-harvesting nanotubes ( $b = 2 \pm 0.5$ ) and pseudocyanine ( $b = 3.4$ ).<sup>48,55</sup>

Changes in linewidths arise from the coupling of exciton degrees of freedom (system) to vibrational degrees of freedom (environment/phonon bath). Specifically, under the weak-coupling, fast-environment limit, the power-law exponent ( $b$ ) of the temperature dependent linewidth can be broken down as  $b = d + s + 1$ , where  $d$  and  $s$  are the scaling of the exciton DOS at the band edge, and low-frequency system-bath coupling spectral density, respectively.<sup>52,53,56</sup>  $s = 1$  for an Ohmic bath while  $s < 1$  for a subohmic bath. A similar expression can be derived for temperature dependent peak shifts, which reflects the same underlying band structure (see [supplementary material Sec. 3](#)).<sup>34</sup> For 2D excitonic systems with non-nearest neighbor dipole–dipole couplings, the system DOS scaling has been shown to follow a  $d = 0.5$  dependence.<sup>57</sup> Thus, we obtain  $s = 0$  for TDBC and  $s \sim -0.5$  for the rest of the benzothiazole Cy3 and Cy5 aggregates indicating that the system-bath coupling spectral density in the TDBC aggregate is independent of frequency while the negative sign for the rest of the band edge aggregates indicates an inverse scaling. The scaling laws may be explained by the fact that the excitonic couplings in these systems are quite large ( $\sim 10^3 \text{ cm}^{-1}$ ), and the higher frequency components of system-bath coupling will be highly suppressed in comparison. For finite coherent length, pure dephasing may compete with population relaxation and lead to linear scaling with temperature.<sup>56</sup> Although, this is unlikely in our case, since all aggregates had up to micrometer scale sizes as seen from cryoEM images ([supplementary material Fig. S3](#)).<sup>39</sup>

### Screening aggregate geometries using stochastic modeling of the Hamiltonian

In [Figs. 5\(a\)](#) and [5\(b\)](#), we show the exciton bandwidth and position of  $k = 0$  bright state as a function of slip for zero disorder case for different dipolar coupling models, obtained using the procedure in [supplementary material, Sec. 2](#). We observe significant differences in the slip dependent properties of the excitonic band structure depending on the coupling model as well as the aggregate packing geometry. The use of an extended dipole model opens up a larger range of slips, which show I-aggregate behavior. We attribute this to the point dipole model that shows a steeper slip dependence overestimating the short-range couplings (as seen in [supplementary material, Fig. S1b](#)) and, therefore, results in a very small I-aggregate region. Furthermore, the slip dependence for Cy7-DPA [[Fig. 5\(c\)](#)] shows the effect of longer brick length, where the possible slip range for I-aggregation is expanded further. This is the result of increased positive contributions to the short-range couplings due to longer molecular species.<sup>58</sup> The total bandwidth of the excitonic DOS is bounded by twice the absolute value of the net coupling which has a minimum at zero i.e., when it changes sign from positive to negative. As a result, the exciton bandwidth is minimized around the boundary between I- and J-aggregate regions.

We screen large parameter space of possible aggregate packing parameters (slips) and disorder values using the stochastic sampling methods for the DOS, and Chebyshev kernels the absorption spectra, following Bradbury *et al.*<sup>23</sup> The stochastic density of states is calculated by taking a random superposition of all eigenstates, projecting it down onto a specific energy in the spectrum, and then averaging over many random samplings. This approach is computationally less expensive than diagonalizing large Hamiltonians and allows for rapid screening of several aggregate geometries with realistic sizes ( $\sim 10^6$  monomer

units). Several disorder realizations can be afforded at no additional cost. By screening thousands of configurations for each aggregate, we obtain the slip dependence of the excitonic band and the position of the bright state ( $k = 0$ ). In [supplementary material Fig. S9](#), we show large parameter screens for FWHM and peak positions of all six aggregates. Best fit slip parameters for each aggregate were determined by comparing the calculated spectral widths to the FWHM at 0 K obtained from the power law fits listed in Table S1 i.e., parameter  $c$  from Eq. (3). We narrow down the possible slip–disorder space to the gray squares in [supplementary material Fig. S9](#).

From the narrowed down range of slips (gray squares on [Fig. S9](#)), we use a slip of 5.0 Å and plot the calculated excitonic DOS and absorption spectra in [Fig. 5\(d\)](#). While the realistic slips may be slightly different for each aggregate depending on the central position substitution, we use this representative value as it was consistent with our experimental observations among the narrowed down range of slips. As the brick length increases from Cy3 to Cy7 dyes and relative slip (normalized to brick length) decreases [[Fig. 5\(e\)](#)], we observe that the exciton band structure goes from band edge J-aggregate to mid-band I-aggregate. Our calculations in [Fig. 5\(d\)](#) show that all the Cy3 dyes have a band edge bright state, lower energy than the VHP. This is consistent with our inference from [Tables I](#) and [II](#), based on temperature dependent shifts and emissive properties. Cy5-Ph, while lower energy than the VHP, also has a broad linewidth with significant oscillator strength farther up in the DOS, explaining the suppression of aggregate to monomer quantum yield and the red shifting behavior. Finally, Cy7-Ph and Cy7-DPA both have bright states away from the band edge, explaining the I-aggregate behavior seen in our experiments. Cy7-Ph also has the absorption peak in the relatively flat region of the DOS, consistent with our temperature dependent experiments which showed no shift. While Cy7-DPA appears to have local positive slope at 5.0 Å slip, the realistic slip is higher than that of Cy7-Ph due to a bulkier center position substitution as we have previously shown.<sup>22</sup> This is shown in the bottom two panels of [Fig. 5\(d\)](#), where a higher slip value pushes the bright state in a locally negative slope region of the DOS, explaining the temperature dependent blue shifts. The bottom three panels clearly confirm our inference from [Table II](#) that both the Cy7 aggregates are I-aggregates.

Thus, supramolecular modulation of chromophore packing in 2D aggregates can allow for tunable excitonic band structures where the position of the bright state relative to the band edge and to the VHP can be controlled with slips and molecular lengths. Such dependencies are a direct consequence of the relative contributions of positive and negative couplings afforded by different brick layer geometries. Furthermore, these relations can be exploited to chemically tune the band structures of higher dimensional aggregates and ultimately control the photophysical properties relevant for their applications. J-aggregates can be useful for noninvasive SWIR imaging due to their high quantum yields and narrow linewidths but SWIR aggregates reported so far have very low quantum yields ( $\phi_F < 1\%$ ), possibly because many are, in fact, non-band edge I-aggregates.<sup>11,12</sup> By making SWIR aggregates with higher slips, their bright states can be pushed close to the band edge yielding high quantum yield J-aggregates in SWIR, which could be transformative for SWIR technologies.

We note that our findings are independent of the nature of the couplings and depend mainly on the relative strengths and signs of the short and long-range couplings. Here, we show the importance of

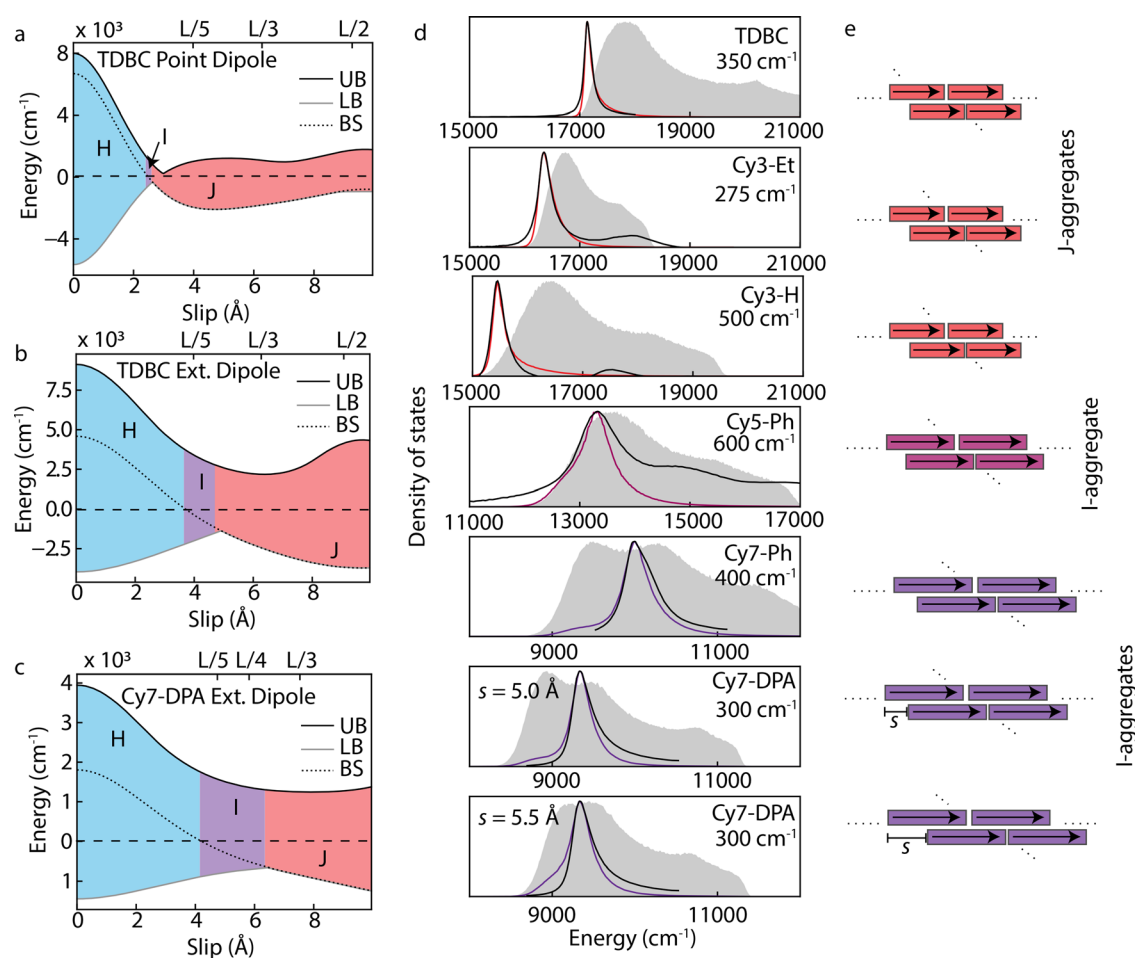


**FIG. 5.** (a)–(c) Slip dependent behavior of the band structure—upper band edge (UB, black line), lower band edge (LB, gray line), and bright state (BS, dotted line) with H-, I-, and J-aggregation regions color coded as blue, violet, and red, respectively, for 2D aggregates of (a) TDBC using point dipole model, (b) TDBC using extended dipole model, (c) Cy7-DPA using extended dipole model. Dashed lines indicate monomer energy, and dotted lines indicate the bright state, (d) calculated excitonic density of states (gray region) and absorption spectra (colored lines) at 0 K for all 2D aggregates with a slip of 5.0 Å (top six panels) and given disorder values. The red shifts of the calculated spectra are adjusted to match the 78 K spectra for each corresponding dye (black lines). The last panel shows the same for Cy7-DPA with higher slip of 5.5 Å, and (e) schematics of the corresponding brick layer geometries.

supramolecular packing parameter in modulating the relative contributions of short and long-range couplings. In addition to the supramolecular geometries, the type of the nearest-neighbor couplings can also be used to modulate the relative contributions from short and long-range couplings, e.g., inclusion of charge-transfer or quadrupolar couplings between the monomers in addition to excitonic couplings. Specifically, Figs. 5(a) and 5(b) show that the point dipole model greatly overestimates the short-range contributions and results in a very small I-aggregate region while the more accurate transition charges model (with partial charges assigned to individual atoms) gives a much larger I-aggregate region for the same geometric parameters.

## CONCLUSIONS

Our work shows that different nanoscale aggregate geometries can be used to avail the vast diversities in the excitonic properties of 2D aggregates. The excitonic band structure of such aggregates can be

experimentally probed using temperature dependent spectroscopy, which forms a comprehensive tool, relating specific experimental observables to distinct aspects of the excitonic band structure. We show temperature dependence studies of six 2D aggregates where carefully chosen dyes with varying brick lengths and central position substitutions afford different aggregate geometries. Different nearest neighbor coupling curves could be realized with charge-transfer interactions (e.g., donor acceptor molecules).<sup>19,20</sup>

Ultimately, the supramolecular tunability of excitonic band structures shown here can be used to rationally design molecular aggregates for specific applications. J-aggregates, with a band edge bright state, have high quantum yields and superradiance rates,<sup>1,14,46</sup> making them great candidates for shortwave infrared imaging,<sup>11,12</sup> polaritonics,<sup>8</sup> and telecommunications.<sup>13</sup> I-aggregates on the other hand, can be interesting for applications involving fast energy or charge transfer in the near-field.<sup>22,59</sup> Such supramolecular tunability of the excitonic band

structure will, therefore, have exciting implications in several fields, including shortwave infrared imaging, excitonic energy transfer, polaritonics, and plexitonics.<sup>5,60</sup>

## SUPPLEMENTARY MATERIAL

See the [supplementary material](#) for experimental section, computational methods, cryoEM, room temperature absorption and emission spectra, lifetimes, temperature dependent absorption and emission spectra, power law fits, derivation of temperature dependent peak shift power law, stochastic screens of aggregate slips, and disorder.

## ACKNOWLEDGMENTS

This work was supported by the NSF CHE under Grant No. 1905242 and Faculty Research Grant (UCLA Academic Senate). N.C.B. and D.N. are grateful for support by the NSF under Grant No. CHE-1763176. A.P.D. thanks UCLA Graduate Division Dissertation Year Fellowship as well as Thomas L and Ruth F Jacobs Award for financial support. N.G. is grateful for a PROMOS stipend granted by Leipzig University, Germany. N.C.B. thanks the NSF-GRFP under Grant No. DGE-2034835. J.C. was supported by the NSF (Grant Nos. CHE 1800301 and CHE 1836913). A.P.D. and J.R.C. thank Professor Benjamin J. Schwartz, UCLA for helpful discussions. A.P.D. thanks Ray Huang for formatting [supplementary material](#) figures. Authors acknowledge the Materials Characterization Laboratory, UCLA Chemistry and Biochemistry for instrumentation.

## AUTHOR DECLARATIONS

### Conflict of Interest

The authors have no conflicts to disclose.

### Author Contributions

**Arundhati P. Deshmukh:** Conceptualization (equal); Data curation (equal); Formal analysis (equal); Investigation (equal); Methodology (equal); Project administration (equal); Supervision (equal); Writing – original draft (equal); Writing – review and editing (equal). **Niklas Geue:** Data curation (equal); Formal analysis (equal); Investigation (equal); Methodology (equal); Writing – review and editing (supporting). **Nadine C. Bradbury:** Formal analysis (equal); Software (equal); Validation (equal); Visualization (equal); Writing – review and editing (equal). **Timothy L. Atallah:** Investigation (supporting); Project administration (supporting); Supervision (supporting); Writing – review and editing (supporting). **Chern Chuang:** Conceptualization (equal); Supervision (equal); Writing – review and editing (equal). **Monica Pengshung:** Methodology (supporting); Resources (supporting). **Jianshu Cao:** Conceptualization (supporting); Resources (supporting). **Ellen M. Sletten:** Conceptualization (equal); Funding acquisition (equal); Resources (equal); Writing – review and editing (equal). **Daniel Neuhauser:** Investigation (supporting); Methodology (supporting). **Justin R. Caram:** Conceptualization (lead); Formal analysis (equal); Funding acquisition (equal); Investigation (supporting); Methodology (equal); Project administration (equal); Resources (equal); Supervision (equal); Writing – original draft (supporting); Writing – review and editing (equal).

## DATA AVAILABILITY

The data that support the findings of this study are available from the corresponding author upon reasonable request.

## REFERENCES

- 1J. L. Bricks, Y. L. Slominskii, I. D. Panas, and A. P. Demchenko, *Methods Appl. Fluoresc.* **6**, 012001 (2017).
- 2T. Brixner, R. Hildner, J. Köhler, C. Lambert, and F. Würthner, *Adv. Energy Mater.* **7**, 1700236 (2017).
- 3C. Wang and E. A. Weiss, *J. Am. Chem. Soc.* **138**, 9557–9564 (2016).
- 4J. W. Oh, S. Kumazaki, I. V. Rubtsov, T. Suzumoto, T. Tani, and K. Yoshihara, *Chem. Phys. Lett.* **352**, 357–362 (2002).
- 5S. K. Saikin, A. Eisfeld, S. Valleau, and A. Aspuru-Guzik, *Nanophotonics* **2**, 21–38 (2013).
- 6B. Kriete, C. J. Feenstra, and M. S. Pshenichnikov, *Phys. Chem. Chem. Phys.* **22**, 10179–10188 (2020).
- 7H. M. Gibbs, G. Khitrova, and S. W. Koch, *Nat. Photonics* **5**, 273–273 (2011).
- 8X. Zhong, T. Chervy, S. Wang, J. George, A. Thomas, J. A. Hutchison, E. Devaux, C. Genet, and T. W. Ebbesen, *Angew. Chem. - Int. Ed.* **55**, 6202–6206 (2016).
- 9A. Eisfeld and J. S. Briggs, *Phys. Status Solidi A* **215**, 1700634 (2018).
- 10S. I. Pozin, D. A. Lypenko, O. M. Perelygina, O. L. Gribkova, V. V. Prokhorov, and E. I. Mal'tsev, *Inorg. Mater. Appl. Res.* **12**, 94–100 (2021).
- 11W. Chen, C. A. Cheng, E. D. Cosco, S. Ramakrishnan, J. G. P. Lingg, O. T. Bruns, J. I. Zink, and E. M. Sletten, *J. Am. Chem. Soc.* **141**, 12475–12480 (2019).
- 12C. Sun, B. Li, M. Zhao, S. Wang, Z. Lei, L. Lu, H. Zhang, L. Feng, C. Dou, D. Yin, H. Xu, Y. Cheng, and F. Zhang, *J. Am. Chem. Soc.* **141**, 19221–19225 (2019).
- 13P. A. Bouit, G. Wetzel, G. Berginc, B. Loiseaux, L. Toupet, P. Feneyrou, Y. Bretonnière, K. Kamada, O. Maury, and C. Andraud, *Chem. Mater.* **19**, 5325–5335 (2007).
- 14S. Doria, T. S. Sinclair, N. D. Klein, D. I. G. Bennett, C. Chuang, F. S. Freyria, C. P. Steiner, P. Foggi, K. A. Nelson, J. Cao, A. Aspuru-Guzik, S. Lloyd, J. R. Caram, and M. G. Bawendi, *ACS Nano* **12**, 4556–4564 (2018).
- 15M. Kasha, *Radiat. Res.* **20**, 55–71 (1963).
- 16M. Kasha, H. R. Rawls, and M. A. El-Bayoumi, *Pure Appl. Chem.* **11**, 371–392 (1965).
- 17I. G. Scheblykin, M. M. Bataiev, M. Van der Auweraer, and A. G. Vitukhnovskiy, *Chem. Phys. Lett.* **316**, 37–44 (2000).
- 18E. W. Knapp, *Chem. Phys.* **85**, 73–82 (1984).
- 19D. Bialas, C. Zhong, F. Würthner, and F. C. Spano, *J. Phys. Chem. C* **123**, 18654–18664 (2019).
- 20C. Zheng, C. Zhong, C. J. Collison, and F. C. Spano, *J. Phys. Chem. C* **123**, 3203–3215 (2019).
- 21A. Eisfeld, C. Marquardt, A. Paulheim, and M. Sokolowski, *Phys. Rev. Lett.* **119**, 097402 (2017).
- 22A. P. Deshmukh, D. Koppel, C. Chuang, D. M. Cadena, J. Cao, and J. R. Caram, *J. Phys. Chem. C* **123**, 18702–18710 (2019).
- 23N. C. Bradbury, C. Chuang, A. P. Deshmukh, E. Rabani, R. Baer, J. R. Caram, and D. Neuhauser, *J. Phys. Chem. A* **124**, 10111–10120 (2020).
- 24H. Yamagata and F. C. Spano, *J. Chem. Phys.* **136**, 184901 (2012).
- 25J. Clark, C. Silva, R. H. Friend, and F. C. Spano, *Phys. Rev. Lett.* **98**, 206406 (2007).
- 26F. C. Spano, *J. Am. Chem. Soc.* **131**, 4267–4278 (2009).
- 27N. J. Hestand and F. C. Spano, *Chem. Rev.* **118**, 7069–7163 (2018).
- 28C. Didraga, A. Pugžlys, P. R. Hania, H. von Berlepsch, K. Duppen, and J. Knoester, *J. Phys. Chem. B* **108**, 14976–14985 (2004).
- 29F. S. Freyria, J. M. Cordero, J. R. Caram, S. Doria, A. Dodin, Y. Chen, A. P. Willard, and M. G. Bawendi, *Nano Lett.* **17**, 7665–7674 (2017).
- 30*In Vivo Self-Assembly Nanotechnology for Biomedical Applications, Nanomedicine and Nanotoxicology*, edited by H. Wang and L.-L. Li (Springer, 2018).
- 31J. H. Kim, T. Schembri, D. Bialas, M. Stolte, and F. Würthner, *Adv. Mater.* **34**, 2104678 (2022).

- <sup>32</sup>K. Sauer, R. J. Cogdell, S. M. Prince, A. Freer, N. W. Isaacs, and H. Scheer, *Photochem. Photobiol.* **64**, 564–576 (1996).
- <sup>33</sup>C. Didraga, J. A. Klugkist, and J. Knoester, *J. Phys. Chem. B* **106**, 11474–11486 (2002).
- <sup>34</sup>C. Chuang, D. I. G. Bennett, J. R. Caram, A. Aspuru-Guzik, M. G. Bawendi, and J. Cao, *Chem* **5**, 3135–3150 (2019).
- <sup>35</sup>V. Czikkely, H. D. Forsterling, and H. Kuhn, *Chem. Phys. Lett.* **6**, 207–210 (1970).
- <sup>36</sup>B. Ghosh, S. Mardanya, B. Singh, X. Zhou, B. Wang, T.-R. Chang, C. Su, H. Lin, A. Agarwal, and A. Bansil, *Phys. Rev. B* **100**, 235101 (2019).
- <sup>37</sup>D. Y. Xing, M. Liu, and C. D. Gong, *Phys. Rev. Lett.* **68**, 1090 (1992).
- <sup>38</sup>G. Li, A. Luican, J. M. B. Lopes Dos Santos, A. H. Castro Neto, A. Reina, J. Kong, and E. Y. Andrei, *Nat. Phys.* **6**, 109 (2010).
- <sup>39</sup>A. P. Deshmukh, A. D. Bailey, L. S. Forte, X. Shen, N. Geue, E. M. Sletten, and J. R. Caram, *J. Phys. Chem. Lett.* **11**, 8026–8033 (2020).
- <sup>40</sup>J. Moll, S. Daehne, J. R. Durrant, and D. A. Wiersma, *J. Chem. Phys.* **102**, 6362–6370 (1995).
- <sup>41</sup>A. V. Sorokin, I. Y. Ropakova, R. S. Grynyov, M. M. Vilksy, V. M. Liakh, I. A. Borovoy, S. L. Yefimova, and Y. V. Malyukin, *Dye Pigm.* **152**, 49–53 (2018).
- <sup>42</sup>M. Müller, A. Paulheim, A. Eisfeld, and M. Sokolowski, *J. Chem. Phys.* **139**, 044302 (2013).
- <sup>43</sup>S. Pascal, A. Haefele, C. Monnereau, A. Charaf-Eddin, D. Jacquemin, B. L. Guennic, C. Andraud, and O. Maury, *J. Phys. Chem. A* **118**, 4038–4047 (2014).
- <sup>44</sup>L. M. Tolbert and X. Zhao, *J. Am. Chem. Soc.* **119**, 3253–3258 (1997).
- <sup>45</sup>M. Eskandari, J. C. Roldao, J. Cerezo, B. Milián-Medina, and J. Gierschner, *J. Am. Chem. Soc.* **142**, 2835–2843 (2020).
- <sup>46</sup>S. Özçelik and D. L. Akins, *J. Phys. Chem. B* **103**, 8926–8929 (1999).
- <sup>47</sup>H. C. Friedman, E. D. Cosco, T. L. Atallah, E. M. Sletten, and J. R. Caram, “Establishing design principles for emissive organic SWIR chromophores from energy gap laws,” *Chem* **7**, 3359–3376 (2021).
- <sup>48</sup>J. R. Caram, S. Doria, D. M. Eisele, F. S. Freyria, T. S. Sinclair, P. Rebentrost, S. Lloyd, and M. G. Bawendi, *Nano Lett.* **16**, 6808–6815 (2016).
- <sup>49</sup>I. G. Scheblykin, O. Y. Sliusarenko, L. S. Lepnev, A. G. Vitukhnovsky, and M. Van Der Auweraer, *J. Phys. Chem. B* **105**, 4636–4646 (2001).
- <sup>50</sup>A. Merdasa, Á. J. Jiménez, R. Camacho, M. Meyer, F. Würthner, and I. G. Scheblykin, *Nano Lett.* **14**, 6774–6781 (2014).
- <sup>51</sup>T. E. Kaiser, I. G. Scheblykin, D. Thomsson, and F. Wu, *J. Phys. Chem. B* **113**, 15836–15842 (2009).
- <sup>52</sup>D. J. Heijs, V. A. Malyshev, and J. Knoester, *J. Chem. Phys.* **123**, 144507 (2005).
- <sup>53</sup>D. J. Heijs, V. A. Malyshev, and J. Knoester, *Phys. Rev. Lett.* **95**, 177402 (2005).
- <sup>54</sup>R. W. Mattoon, *J. Chem. Phys.* **12**, 268 (2004).
- <sup>55</sup>I. Renge and U. P. Wild, *J. Phys. Chem. A* **101**, 7977–7988 (1997).
- <sup>56</sup>A. G. Dijkstra, H.-G. Duan, J. Knoester, K. A. Nelson, and J. Cao, *J. Chem. Phys.* **144**, 134310 (2016).
- <sup>57</sup>C. Chuang and J. Cao, *Phys. Rev. Lett.* **127**, 047402 (2021).
- <sup>58</sup>B. P. Krueger, G. D. Scholes, and G. R. Fleming, *J. Phys. Chem. B* **102**, 5378–5386 (1998).
- <sup>59</sup>X. Gao and A. Eisfeld, *J. Phys. Chem. Lett.* **9**, 6003–6010 (2018).
- <sup>60</sup>K. Chevrier, J. M. Benoit, C. Symonds, J. Papparone, J. Laverdant, and J. Bellessa, *ACS Photonics* **5**, 80–84 (2018).